University of Amsterdam

Extended Power-Law Decays in BATSE Gamma-Ray Bursts: Signatures of External Shocks?

Giblin, T.W.; Connaughton, V.; van Paradijs, J.A.; Preece, R.D.; Briggs, M.S.; Kouveliotou, C.; Wijers, R.A.M.J.; Fishman, G.J.

EXTENDED POWER-LAW DECAYS IN BATSE GAMMA-RAY BURSTS: SIGNATURES OF EXTERNAL SHOCKS?

T. W. GIBLIN,[1,2,3] V. CONNAUGHTON,[1,2] J. VAN PARADIJS,[1,4,5] R. D. PREECE,[1,2] M. S. BRIGGS,[1,2]
C. KOUVELIOTOU,[2,6] R. A. M. J. WIJERS,[7] AND G. J. FISHMAN[2]

ABSTRACT

The connection between gamma-ray bursts (GRBs) and their afterglows is currently not well understood. Afterglow models of synchrotron emission generated by external shocks in the GRB fireball model predict emission detectable in the gamma-ray regime ($\gtrsim 25$ keV). In this paper, we present a temporal and spectral analysis of a subset of BATSE GRBs with smooth extended emission tails to search for signatures of the "early high-energy afterglow," i.e., afterglow emission that initially begins in the gamma-ray phase and subsequently evolves into X-ray, UV, optical, and radio emission as the blast wave is decelerated by the ambient medium. From a sample of 40 GRBs we find that the temporal decays are best described with a power law $\sim t^{\beta}$ rather than an exponential with a mean index $\langle \beta \rangle \approx -2$. Spectral analysis shows that $\sim 20\%$ of these events are consistent with fast-cooling synchrotron emission for an adiabatic blast wave, three of which are consistent with the blast-wave evolution of a jet with $F_{\nu} \sim t^{-p}$. This behavior suggests that in some cases, the emission may originate from a narrow jet, possibly consisting of "nuggets" whose angular sizes are less than $1/\Gamma$, where Γ is the bulk Lorentz factor.

Subject heading: gamma rays: bursts

1. INTRODUCTION

Afterglow emissions from gamma-ray bursts (GRBs) in the X-ray, optical, and radio wave bands are in good agreement with afterglow models of relativistic fireballs (Wijers, Rees, & Mészáros 1997; Galama et al. 1998; Waxman 1997; Vietri 1997). The observed afterglow spectrum is well described as synchrotron emission that arises from the interaction of the relativistic blast wave with bulk Lorentz factor $\Gamma_0 \sim 10^2$–10^3 with the ambient medium (Mészáros & Rees 1997; Galama et al. 1998). The often highly variable gamma-ray phase of the burst may reflect the physical behavior of the fireball progenitor through collisions internal to the flow, i.e., internal shocks (Sari & Piran 1997; Kobayashi, Piran, & Sari 1997). On the other hand, Dermer & Mitman (1999) have suggested a blast wave with an inhomogenous external medium. Heinz & Begelman (1999) have suggested an inhomogeneous bullet-like jet outflow that encounters the interstellar medium.

The precise relationship between the observed GRB and the afterglow emission is not well understood. GRBs recorded by the *BeppoSAX* satellite suggest that the X-ray afterglow emission may be delayed in time from the main GRB (e.g., GRB 970228; Costa 2000) or may begin during the GRB emission (e.g., GRB 980519; in't Zand et al. 1999).

In the latter case, it is not clear if the X-ray afterglow is a separate underlying emission component or a continuation of the GRB itself. The internal-external shock model presents a scenario in which emission from internal and external shocks may overlap in time. If the internal shocks reflect the activity of the progenitor, then the onset of the afterglow may be separated from the prompt gamma-ray emission. Since the nature of the progenitor is not known, the effect of the ambient medium on the emission from the progenitor is highly problematic. The model therefore does not prohibit internal and external shock emissions from overlap, while in other cases the afterglow emission may be delayed with respect to the GRB (see, e.g., Sari & Piran 1999; Mészáros & Rees 1999; Vietri 2000).

The detection of optical emission simultaneous with the gamma-ray emission of GRB 990123 (Akerlof et al. 1999) provided the first evidence for two distinct emission components in a GRB; here the prompt optical emission is believed to originate from synchrotron emission in the production of the reverse shock generated when the ejecta encounters the external medium (Galama et al. 1999; Sari & Piran 1999; Mészáros & Rees 1999). The gamma-ray spectrum of GRB 990123 cannot be extrapolated from the spectral flux from the simultaneous optical emission, indicating that the optical and gamma-ray emission originate from two separate mechanisms (Briggs et al. 1999; Galama et al. 1999). Evidence for overlapping shock emission was also found in GRB 980923 (Giblin et al. 1999b), where a long power-law decay tail ($\sim t^{-1.8}$) was observed in soft gamma rays (25–300 keV). Two separate emission components are favored in this burst because the spectral characteristics of the tail were markedly different from those of the variable main GRB emission. The spectrum in the tail is consistent with that of a slow-cooling synchrotron spectrum, similar to the behavior of low-energy afterglows (see, e.g., Bloom et al. 1998; Vreeswijk et al. 1999).

[1] Department of Physics, University of Alabama in Huntsville, Huntsville, AL 35899.

[2] NASA Marshall Space Flight Center, SD50, Huntsville, AL 35812.

[3] New address: Department of Physics and Astronomy, College of Charleston, 58 Coming Street, Charleston, SC 29424.

[4] Astronomical Institute "Anton Pannekoek," University of Amsterdam; and Center for High Energy Astrophysics, Kruislaan 403, 1098 SJ Amsterdam, Netherlands.

[5] Deceased.

[6] Universities Space Research Association.

[7] Department of Physics and Astronomy, State University of New York at Stony Brook, Stony Brook, NY 11794-3800.

The gamma rays produced by internal shocks and the soft gamma rays of the "afterglow" may therefore overlap, the latter having a signature of power-law decay in the synchrotron afterglow model. If this is the case, at least some GRBs in the BATSE database should show signatures of the early external shock emission. These events would contain a soft gamma-ray (or hard X-ray) tail component that decays as a power law in their time histories, possibly superposed on the variable gamma-ray emission. It has been shown that the peak frequency of the initial synchrotron emission, which depends on the parameters of the system (see § 2), can peak in hard X-rays or gamma rays (Rees & Mészáros 1992). Further, it may be possible to see a smoothly decaying GRB that is the result of an external shock; i.e., the GRB itself is a "high-energy" afterglow. For such GRBs, the subsequent afterglow emission in X-rays and optical would then simply be the evolution of the burst spectrum. A situation like this might arise when the progenitor generates only a single energy release (i.e., no internal shocks).

It is well known that the temporal structures of GRBs are very diverse and often contain complex, rapid variability. However, some bursts exhibit smooth decay features that persist on timescales as long as, or even longer than, the variable emission of the burst. Our investigation focuses on the combined temporal and spectral behavior of a sample of 40 BATSE GRBs that exhibit smooth decays during the later phase of their time histories. Many of these events fall into a category of bursts traditionally referred to as fast rise, exponential decay bursts (FREDs) with rapid rise times and a smooth extended decay (Kouveliotou et al. 1992). In § 2 we present temporal and spectral properties of the afterglow synchrotron spectrum. In § 3 we examine the temporal behavior and spectral characteristics of the decay emission for the events in our sample and compare their spectra with the model synchrotron spectrum. A color-color diagram (CCD) technique is also applied to systematically explore the spectral evolution of each event. In § 4 we present a set of high-energy afterglow candidates followed by a discussion of our results in the framework of current fireball models.

2. SYNCHROTRON SPECTRA FROM EXTERNAL SHOCKS

Internal shocks are capable of liberating some fraction of the total fireball energy $E_0 = \Gamma_0 M_0 c^2$, leaving a significant fraction to be injected into the external medium via the external shock (Kobayashi et al. 1997). However, recent simulations suggest that internal shock efficiencies can approach $\sim 100\%$ (Beloborodov 2000). Nonetheless, as the blast wave sweeps up the external medium, it produces a relativistic forward shock and a mildly relativistic reverse shock in the opposite direction of the initial flow. The reverse shock decelerates the ejecta, while the forward shock continuously accelerates the electrons into a nonthermal distribution of energies described by a power law $dn_e/d\gamma_e \propto \gamma_e^{-p}$, where γ_e is the electron Lorentz factor. The distribution has a low-energy cutoff given by $\gamma_m \leq \gamma_e$. Behind the shock, the accelerated electrons and magnetic field acquire some fraction ϵ_e and ϵ_B, respectively, of the internal energy.

The resulting synchrotron spectrum of the relativistic electrons consists of four power-law regions (Sari, Piran, & Narayan 1998) defined by three critical frequencies ν_a, ν_c, and ν_m, where ν_a is the self-absorption frequency, $\nu_c = \nu(\gamma_c)$ is the cooling frequency, and $\nu_m = \nu(\gamma_m)$ is the characteristic synchrotron frequency (see Fig. 1 in Sari et al. 1998). Here we are only concerned with the high-energy spectrum; therefore, we do not consider self-absorption. Electrons with $\gamma_e \geq \gamma_c$ cool down to γ_c, the Lorentz factor of an electron that cools on the hydrodynamic timescale of the shock (Piran 1999). The electrons cool rapidly when $\gamma_m \geq \gamma_c$, known as *fast cooling* (i.e., $\nu_m > \nu_c$), and cool more slowly when $\gamma_m \leq \gamma_c$, known as *slow cooling*. In the fast-cooling regime, the evolution of the shock may range from fully radiative ($\epsilon_e \sim 1$) to fully adiabatic ($\epsilon_e \ll 1$). In the slow-cooling mode, the evolution can only be adiabatic since $\gamma_m < \gamma_c$. The characteristic synchrotron frequency of an electron with minimum Lorentz factor γ_m is (Sari & Piran 1999)

$$\nu_m = 1.0 \times 10^{19} \text{ Hz} \left(\frac{\epsilon_e}{0.1}\right)^2 \left(\frac{\epsilon_B}{0.1}\right)^{1/2} \left(\frac{\Gamma}{300}\right)^4 n_1^{1/2} , \quad (1)$$

corresponding to a break in the observed spectrum with energy

$$E_m = 41.4 \text{ keV} \left(\frac{\epsilon_e}{0.1}\right)^2 \left(\frac{\epsilon_B}{0.1}\right)^{1/2} \left(\frac{\Gamma}{300}\right)^4 n_1^{1/2} , \quad (2)$$

where Γ is the bulk Lorentz factor and n_1 is the constant density of the ambient medium. Although the frequency in equation (1) depends strongly on the parameters of the system, the forward shock may very well peak initially in hard X-rays or in gamma rays (Sari & Piran 1999).

The synchrotron spectrum evolves with time according to the hydrodynamic evolution of the shock and the geometry of the fireball (e.g., spherical or collimated). Specifically, the time dependence of ν_c and ν_m will strongly depend on the time evolution of the Lorentz factor $\gamma(t)$. Assuming a spherical blast wave and a homogeneous medium, for radiative fast cooling, $\nu_m \propto t^{-12/7}$ and $\nu_c \propto t^{-2/7}$, while for adiabatic evolution (fast or slow cooling), $\nu_m \propto t^{-3/2}$ and $\nu_c \propto t^{-1/2}$. The shape of the synchrotron spectrum remains constant with time as ν_c and ν_m evolve to lower values. In the fast-cooling mode, ν_m decays faster than ν_c, causing a transition in the spectrum from fast to slow cooling.

Since the break frequencies scale with time as a power law, the spectral energy flux of the synchrotron spectrum F_ν (in units of ergs s^{-1} cm^{-2} keV^{-1}) will also scale as a power law in time so that $F_\nu(\nu, t) \propto \nu^\alpha t^\beta$, where the spectral and temporal power-law indices α and β depend on the temporal ordering of ν_c relative to ν_m, i.e., fast or slow cooling. For radiative fast cooling,

$$F_\nu \propto \begin{cases} \nu^{1/3} t^{-1/3} , & \nu < \nu_c , \\ \nu^{-1/2} t^{-4/7} , & \nu_c < \nu < \nu_m , \\ \nu^{-p/2} t^{(2-6p)/7} , & \nu_m < \nu , \end{cases} \quad (3)$$

and for adiabatic fast cooling,

$$F_\nu \propto \begin{cases} \nu^{1/3} t^{1/6} , & \nu < \nu_c , \\ \nu^{-1/2} t^{-1/4} , & \nu_c < \nu < \nu_m , \\ \nu^{-p/2} t^{(2-3p)/4} , & \nu_m < \nu \end{cases} \quad (4)$$

(Sari et al. 1998). For slow cooling, the spectral energy flux

is

$$F_\nu \propto \begin{cases} \nu^{1/3} t^{1/2} , & \nu < \nu_m , \\ \nu^{-(p-1)/2} t^{-3(p-1)/4} , & \nu_m < \nu < \nu_c , \\ \nu^{-p/2} t^{-(3p-2)/4} , & \nu_c < \nu \end{cases} \quad (5)$$

(Sari et al. 1998). Note that a simple relation exists between the temporal and spectral indices through the value of the electron index p for the high-energy spectral slopes ($\nu > \nu_c$) and the spectral slope below ν_c in the slow-cooling regime. Defining the low-energy spectral slope as α and the high-energy spectral slope as α', the following relations between the temporal and spectral indices for a spherical blast wave are established (Sari et al. 1998):

$$\beta = \begin{cases} 2(6\alpha' + 1)/7 & \text{(fast cooling, radiative)} , \\ 3\alpha'/2 + 1/2 & \text{(fast cooling, adiabatic)} , \\ 3\alpha/2 & \text{(slow cooling, } \nu_m < \nu < \nu_c) , \\ 3\alpha'/2 + 1/2 & \text{(slow cooling, } \nu_c < \nu) . \end{cases} \quad (6)$$

The numerical value of p is readily determined from the measured high-energy spectral slope, $p = -2\alpha'$. Long-wavelength afterglow measurements give typical electron indices in the range $2.0 \leq p \leq 2.5$. Although the nature of the emission in this model is always synchrotron radiation with its characteristic slopes and breaks, the time dependence of the breaks is affected by the details of the geometry and dynamics.

The relations in equation (6) are only valid in the case of a spherical blast wave encountering a constant density medium. Rhoads (1999) considered the adiabatic evolution of a collimated or jetlike outflow in which the ejecta are confined to a conical volume with a half-opening angle θ_c. As the outflow encounters the external medium, the bulk Lorentz factor of the flow Γ decreases with radius and time as a power law (see, e.g., Huang, Dai, & Lu 1999). However, the hydrodynamical evolution of the shock changes from a power law to an exponential regime when $\theta_b \equiv \Gamma^{-1} \simeq \theta_c$ (Rhoads 1999; Sari, Piran, & Halpern 1999). The observer is able to discern that the flow is confined to an expanding cone rather than a sphere because less radiation is observed. In consequence, a break in the light curve to an $F_\nu \sim t^{-p}$ behavior is observed as the ejecta sweep up a larger amount of mass. For the adiabatic evolution of a jet, $\nu_m \propto t^{-2}$, $\nu_c \propto t^0 = \text{const}$, and the peak flux scales as $F_{\nu,\text{max}} \propto t^{-1}$ (Rhoads 1999; Sari et al. 1999). Thus, the spectral flux for an adiabatic jet in the fast-cooling regime is given by

$$F_\nu \propto \begin{cases} \nu^{1/3} t^{-1} , & \nu < \nu_c , \\ \nu^{-1/2} t^{-1} , & \nu_c < \nu < \nu_m , \\ \nu^{-p/2} t^{-p} , & \nu > \nu_m , \end{cases} \quad (7)$$

and for slow cooling by

$$F_\nu \propto \begin{cases} \nu^{1/3} t^{-1/3} , & \nu < \nu_m , \\ \nu^{-(p-1)/2} t^{-p} , & \nu_m < \nu < \nu_c , \\ \nu^{-p/2} t^{-p} , & \nu > \nu_c . \end{cases} \quad (8)$$

The jet geometry can therefore be tested by the simple relation $\beta = 2\alpha' = -p$, irrespective of whether the spectrum is fast- or slow-cooling, provided that $\nu > \max(\nu_c, \nu_m)$.

3. ANALYSIS

We examine the properties of extended decay emission in GRBs in the energy range ~25–2000 keV using data from BATSE, a multidetector all-sky monitor instrument on board the *Compton Gamma Ray Observatory* (*CGRO*). BATSE consisted of eight identical detector modules placed at the corners of the *CGRO* in the form of an octahedron (Fishman et al. 1989). Each module contains a large-area detector (LAD) composed of a sodium iodide crystal scintillator that continuously recorded count rates in 1.024 and 2.048 s time intervals with four and 16 energy channels, respectively (known as the DISCLA and CONT data types). Nominally, a burst trigger is declared when the count rates in two or more LADs exceed the background count rate by at least 5.5 σ. Various burst data types are then accumulated, including the four-channel high time resolution (64 ms) discriminator science data (DISCSC). The DISCSC and DISCLA rates cover four broad energy channels in the 25–2000 keV range (25–50, 50–100, 100–300, and >300 keV). The CONT data span roughly the same energy range but with 16 energy channels and 2.048 s time resolution.

3.1. *Data Set and Background Modeling*

Our data set was collected by visually selecting events from the current BATSE catalog with extended decay features using DISCSC time histories in the 25–2000 keV range. Time histories used in this search had a time resolution of 64 ms or longer; therefore, our scan was not sensitive to the selection of events from the short class of bursts in the bimodal duration distribution (Kouveliotou et al. 1993a). A study of decay emission in short GRBs will not be included in this analysis but will be the subject of future work. Our search resulted in a sample of 40 bursts, 17 with a FRED-like profile and 23 that exhibit a period of variability followed by a smooth decaying emission tail.

We grouped events into three categories based on the characteristic time history of the bursts: (1) pure FREDs (PFs), (2) FREDs with initial variability mainly during the peak (FV), and (3) bursts with a period of variability followed by an emission tail (V + T). Note that this categorization only serves as a descriptive guideline for this analysis and does not imply a robust temporal classification scheme. Our analysis uses discriminator (DISCSC and DISCLA) and continuous (CONT) data from the BATSE LADs.

The source count rates in the ith time bin and the jth energy channel $S_{i,j}$ were obtained by subtracting the background model rates $B_{i,j}$ from the burst time history. The background model rates in the jth energy channel were generated by modeling pre- and postburst background intervals appropriate for each burst with a polynomial on the order of n, where $1 \leq n \leq 4$. Postburst intervals were chosen at sufficiently late times beyond the tail of the burst since the time when the tail emission disappears into the background is somewhat uncertain. This method was adequate for bursts with durations less than ~200 s. For longer bursts, however, the long-term variations in the background can inhibit knowledge of when the tail emission drops below the background level. For this reason, we applied an orbital background subtraction method to events with durations that exceed ~200 s. This technique uses as background the average of the CONT data count rates registered when *CGRO*'s orbital position is at the point closest in geomagnetic latitude to that at the time of the burst on days before

and after the burst trigger. A complete description of the technique is given in Connaughton (2002).

3.2. *Temporal Modeling*

In the context of afterglow models, the decay emission is usually fitted with a power law. We fit the smooth decay of the background subtracted source count rates S_i in each burst with a power-law function of the form

$$R(t_i) = R_0(t_i - t_0)^\beta , \qquad (9)$$

where $R(t_i)$ is the model count rate of the ith time bin. The free parameters of the model are the amplitude R_0 in units of counts per second, the power-law index β, and the fiducial point of divergence t_0, given in seconds. As a general guideline, the fit intervals $[\tau_1, \tau_2]$ were selected in a systematic manner. For the PF bursts, the start time of each fit interval τ_1 was taken as the time of half-width at half-maximum intensity of the burst. This approach obviously does not apply to the V + T group of bursts. For these events, τ_1 was defined as the bin following the apparent end time of the variable emission. The fit interval end time τ_2 was defined as the time when the amplitude of the tail count rates first falls within 1 $\sigma_{b, i}$ of the background model, where $\sigma_{b, i}$ is the Poisson count rate uncertainty of the ith bin of the background model. To avoid obtaining a premature value of τ_2 caused by statistical fluctuations in the tail, the amplitude of the count rates in the tail was calculated using a moving average of 16 time bins. The value of τ_2 was not particularly sensitive to the width of the moving average. We further found that the fitted model parameter values were generally insensitive to arbitrarily larger values of τ_2.

The model was fit to the data using a Levenberg-Marquardt nonlinear least-squares χ^2 minimization algorithm. The algorithm was modified to incorporate model variances rather than data variances in the computation of the χ^2 statistic to avoid overweighting data points with strong d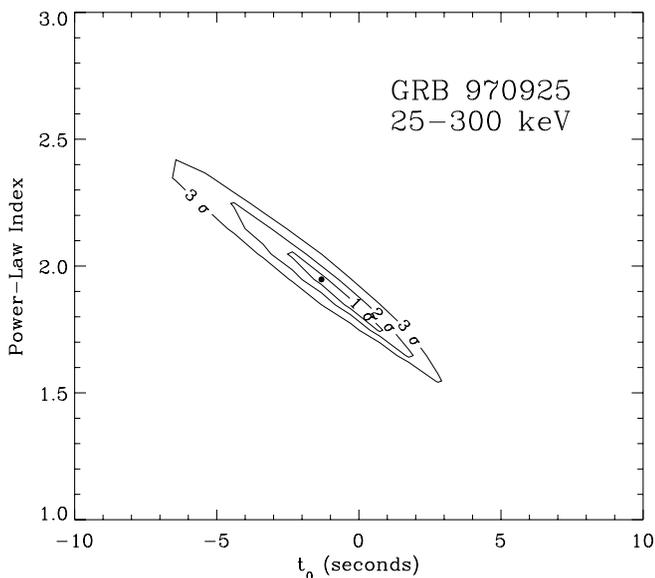ownward Poisson fluctuations (Ford et al. 1995). We performed a set of Monte Carlo simulations to test the accuracy of our fitting method. We found a bias in the distribution of fitted slopes that was hinged on the correlation of the (β, t_0) model parameters. The bias results when the value of τ_1 is too far out in the tail of the power law. In this situation, the curvature of the power-law decay is undersampled and results in a broad χ^2 minimum. The broad χ^2 minimum is most easily illustrated by plotting the joint confidence intervals between β and t_0. For example, Figure 1 shows the $\Delta\chi^2$ contours for the fit to GRB 970925 with $\Delta\chi^2 = 2.3$, 6.2, and 11.8, corresponding to the 68% (1 σ), 95% (2 σ), and 99% (3 σ) confidence levels, respectively, for two parameters of interest (Press et al. 1992, p. 697).

Examples of three burst decays from our sample are displayed in Figure 2. The dashed lines indicate the best-fit power-law model for each event as listed in Table 1. The temporal fit parameters for all events in our sample are given in Table 1. The uncertainties in the β and t_0 parameters quoted in Table 1 reflect the projection of the 68% confidence contours onto the axis of the parameter of interest and, in nearly all cases, are larger than the uncertainties obtained from the covariance matrix in the Levenberg-Marquardt algorithm. It is important to point out that modeling of the temporal decay of afterglow measurements at very

FIG. 1.—$\Delta\chi^2$ contour plot for GRB 970925 that shows the correlation between β and t_0. The elliptical contours are the 1 σ (68%), 2 σ (95%), and 3 σ (99%) joint confidence intervals. Values of β and t_0 corresponding to the fitted χ^2 minimum are indicated by the filled circle.
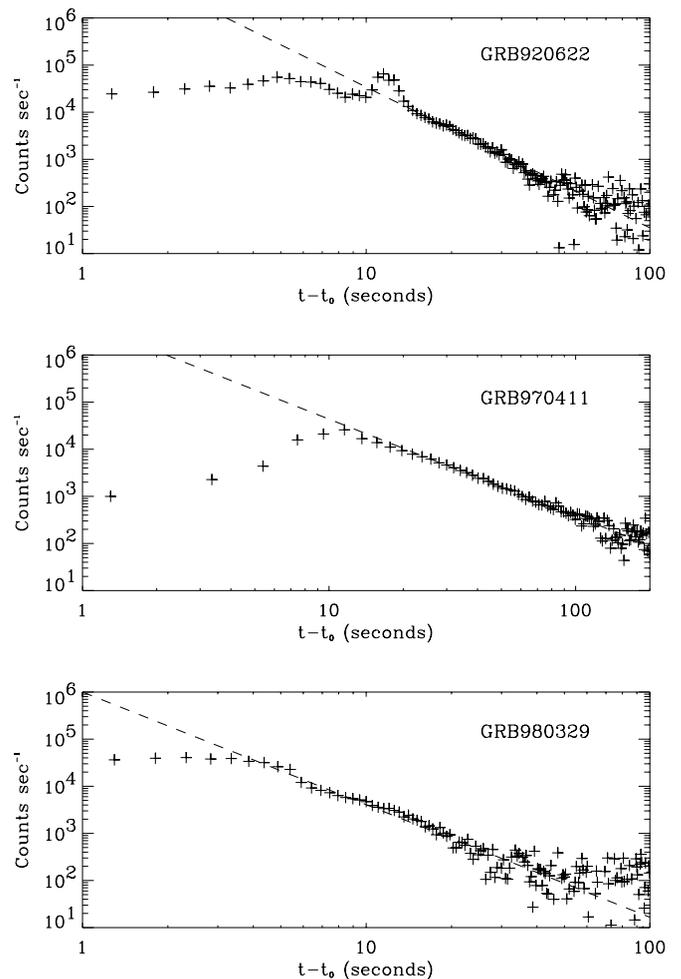

FIG. 2.—Logarithmic plot of the time histories of three events in the 25–300 keV range. The dashed line is the best-fit power-law model for each burst. The time intervals for each fit are listed in the fourth column in Table 1.

TABLE 1

Summary of Temporal Fits (25–300 keV)

GRB	Trigger	Time Profile[a]	$[\tau_1, \tau_2]$ (s)	β	t_0	dof	χ^2 / dof
910602	257	FV	[19, 361]	$-1.74^{-0.72}_{+0.11}$	$-13.69^{-22.58}_{+4.41}$	166	1.41
910814c	676	V + T	[67, 109]	$-1.75^{-0.65}_{+0.40}$	$58.05^{-3.07}_{+2.05}$	39	0.98
910927	829	FV	[15, 52]	$-2.06^{-0.72}_{+0.44}$	$7.69^{-2.14}_{+2.05}$	34	1.20
911016	907	FV	[140, 292]	<-2.06	<113.73	147	4.03
920218	1419	FV	[130, 204]	$-2.15^{-0.54}_{+0.33}$	$120.90^{-1.02}_{+2.08}$	71	1.32
920502	1578	FV	[14, 99]	$-2.51^{-3.27}_{+0.22}$	$4.69^{-17.71}_{+1.10}$	81	1.04
920622	1663	V + T	[21, 80]	<-2.98	<4.77	56	1.75
920801	1733	PF	[9, 123]	$-1.91^{-0.56}_{+0.33}$	$-2.84^{-2.49}_{+3.06}$	110	2.15
920813	1807	FV	[39, 150]	$-2.10^{-6.05}_{+0.04}$	$18.07^{-118.1}_{+0.47}$	106	1.57
920901	1885	PF	[19, 200]	<-2.02	<-12.81	175	1.15
921207	2083	FV	[12, 56]	$-2.88^{-0.03}_{+0.02}$	$3.74^{-0.03}_{+0.02}$	41	1.32
930106	2122	FV	[28, 503]	$-1.76^{-0.33}_{+0.12}$	$-12.28^{-9.23}_{+5.08}$	213	0.88
930131	2151	V + T	[3, 96]	$-0.71^{-0.31}_{+0.11}$	$-2.41^{-4.76}_{+2.12}$	89	0.91
930612	2387	PF	[17, 264]	$-2.09^{-0.86}_{+0.11}$	$1.01^{-9.46}_{+1.48}$	190	1.24
931223	2706	PF	[10, 72]	$-2.57^{-6.71}_{+0.10}$	$-4.75^{-60.4}_{+1.03}$	59	1.26
940218	2833	FV	[7, 50]	$-3.28^{-0.08}_{+0.04}$	$-0.83^{-0.05}_{+0.03}$	40	1.60
940419b	2939	PF	[17, 264]	<-1.75	<-17.48	239	1.51
941026	3257	PF	[17, 131]	<-1.95	<-8.89	109	1.67
951104	3893	V + T	[22, 99]	$-1.97^{-0.22}_{+0.02}$	$14.49^{-0.05}_{+1.03}$	75	1.08
9605301[b]	5478	PF	[9, 121]	$-1.49^{-0.77}_{+0.04}$	$2.36^{-6.38}_{+0.29}$	108	0.88
960530(2)[c] ...	5478	PF	[273, 515]	<-2.13	<251.46	234	1.33
970302	6111	PF	[9, 133]	$-1.49^{-0.93}_{+0.11}$	$-0.81^{-10.43}_{+1.15}$	119	1.85
970411	6168	FV	[44, 398]	$-2.06^{-0.21}_{+0.20}$	$16.01^{-0.00}_{+4.23}$	171	0.95
970925	6397	PF	[12, 85]	$-1.98^{-0.31}_{+0.21}$	$-1.65^{-1.02}_{+2.25}$	69	1.71
971127	6504	PF	[11, 198]	$-1.96^{-0.61}_{+0.11}$	$-4.26^{-6.43}_{+1.57}$	180	1.44
971208	6526	PF[d]	[361, 2995]	$-1.34^{-0.11}_{+0.01}$	$-26.34^{-7.05}_{+6.55}$	1047	2.32
980301	6621	PF	[35, 87]	$-2.50^{-1.58}_{+0.05}$	$27.65^{-7.20}_{+0.11}$	48	1.37
980306	6629	FV	[242, 402]	$-1.71^{-0.71}_{+0.50}$	$219.03^{-5.46}_{+9.51}$	154	1.09
980325	6657	PF	[20, 152]	$-2.32^{-5.64}_{+0.04}$	$-7.49^{-102.5}_{+1.58}$	127	2.36
980329	6665	V + T	[16, 59]	<-2.39	<6.64	40	2.48
981203	7247	FV	[60, 851]	$-1.61^{-0.013}_{+0.002}$	$-17.1^{-6.15}_{+2.13}$	384	1.52
981205	7250	FV	[18, 127]	$-1.59^{-1.57}_{+1.20}$	$-10.92^{-14.67}_{+27.72}$	104	0.90
990102	7293	PF	[13, 235]	$-2.14^{-1.36}_{+0.13}$	$-3.7^{-15.71}_{+2.0}$	215	1.14
990220	7403	PF	[17, 196]	$-1.97^{-1.04}_{+0.30}$	$-9.78^{-16.86}_{+6.16}$	85	0.83
990316	7475	PF	[25, 158]	<-2.20	<11.06	128	1.54
990322	7488	PF	[4, 110]	$-0.87^{-0.02}_{+0.01}$	$1.27^{-0.05}_{+0.13}$	102	1.17
990415	7520	V + T	[44, 122]	<-2.23	<29.44	75	1.54
990518	7575	V + T	[177, 291]	$-1.92^{-0.92}_{+0.90}$	$154.57^{-0.79}_{+15.76}$	110	1.61
991216	7906	V + T	[35, 75]	$-2.35^{-1.15}_{+0.03}$	$26.76^{-6.25}_{+0.00}$	37	1.23
991229	7925	FV	[16, 154]	<-2.09	<-24.29	132	1.16
000103	7932	V + T	[53, 250]	$-1.90^{-1.10}_{+0.90}$	$18.46^{-7.22}_{+24.58}$	191	1.39

[a] Abbreviations for time profile descriptions: PF = pure FRED (i.e., single smooth pulse); FV = FRED with multiple pulses near the peak; V+T = variability+tail.
[b] First emission episode of trigger 5478.
[c] Second emission episode of trigger 5478.
[d] The longest duration GRB observed by BATSE (~3000 s).

late times after the burst (e.g., days, weeks, and months) in, for example, the optical band does not suffer from this bias because the value of t_0 is typically set to the trigger time of the burst, i.e., a very good approximation to the true value of t_0 relative to the time of the fit interval (see, e.g., Fruchter et al. 1999). In the case of the early decays in GRBs, however, the fit is very sensitive since we are fitting so close in time to the burst trigger.

For completeness, we also modeled the decay interval in each event with an exponential function of the form $R_e(t_i) \sim \exp[-(t_i - \tau_1)/\tau_e]$ with the amplitude and exponential decay constant τ_e as free parameters. We find that only 12 of the 41 fits resulted in a lower reduced χ^2-value χ^2_r than that of the power-law model. The largest value of $\Delta\chi^2_r$ of these events was only 1.15, while most other events had $\Delta\chi^2_r \sim 0.3$ or less, indicating that the power law is nearly as good a fit as the exponential. For events in which the exponential model was a poor fit, the power-law fits were strongly favored with $\Delta\chi^2_r$-values as high as 7.5. Our results are consistent with that of a similar study for a small number of GRBs performed early in the BATSE mission (Schaefer & Dyson 1995).

3.3. Spectral Modeling

Nearly all GRB spectra are adequately modeled with a low- and high-energy power-law function smoothly joined over some energy range within the BATSE energy bandpass (Band et al. 1993; Preece et al. 2000). Curvature in the spectrum is almost always observed, although on rare occasions

TABLE 2
Time-integrated Spectral Fits: Smoothly Broken Power Law

GRB	α[a]	α'[a]	E_b (keV)	χ^2 / dof	Δ	p	Category[b]
910927	0.06 ± 0.04	−3.27 ± 0.17	158 ± 7	1.84	3.33 ± 0.17	6.54 ± 0.17	...
920218	−0.69 ± 0.01	−1.45 ± 0.05	175 ± 7	2.37	0.76 ± 0.15	2.90 ± 0.05	...
920502	−0.10 ± 0.05	−1.96 ± 0.20	183 ± 20	1.22	1.86 ± 0.21	3.92 ± 0.20	...
920622	−0.49 ± 0.04	−1.48 ± 0.26	263 ± 68	1.97	0.99 ± 0.26	2.96 ± 0.26	(i), (iii)
920801	−0.23 ± 0.05	−0.98 ± 0.15	252 ± 70	1.13	0.75 ± 0.16	1.96 ± 0.15	(iii)
930612	−0.01 ± 0.17	−1.46 ± 0.12	108 ± 19	0.49	1.45 ± 0.21	2.92 ± 0.12	...
931223	−0.24 ± 0.06	−1.39 ± 0.13	141 ± 12	1.28	1.15 ± 0.14	2.79 ± 0.13	...
940419b	−0.52 ± 0.17	−1.66 ± 0.55	140 ± 73	1.15	1.14 ± 0.58	3.32 ± 0.55	(i)
941026	−0.24 ± 0.03	−1.55 ± 0.08	150 ± 6	2.32	1.32 ± 0.09	3.10 ± 0.08	...
9605301........	−0.10 ± 0.18	−1.48 ± 0.22	128 ± 33	1.59	1.47 ± 0.28	2.96 ± 0.22	...
960530(2)	−0.56 ± 0.04	−1.88 ± 0.37	203 ± 25	1.54	1.33 ± 0.37	3.76 ± 0.37	(i)[c]
970411	−0.35 ± 0.04	−1.10 ± 0.08	228 ± 41	1.60	0.75 ± 0.09	2.20 ± 0.08	(iii)
970925	−0.02 ± 0.32	−1.28 ± 0.13	101 ± 32	1.10	1.26 ± 0.35	2.56 ± 0.13	(iii)
971208	−0.55 ± 0.02	−2.03 ± 0.04	179 ± 6	2.02	1.48 ± 0.04	4.06 ± 0.04	...
980301	−0.55 ± 0.22	−1.24 ± 0.13	76 ± 34	0.80	0.69 ± 0.13	2.48 ± 0.13	(i), (iii)
981203	0.29 ± 0.05	−0.59 ± 0.01	124 ± 8	2.28	0.88 ± 0.05	...[d]	(iii)
990102	0.53 ± 0.16	−1.82 ± 0.15	121 ± 14	1.03	2.35 ± 0.22	3.64 ± 0.15	...
990220	0.64 ± 0.24	−1.36 ± 0.08	94 ± 13	5.79	2.00 ± 0.25	2.72 ± 0.08	...
990316	−0.58 ± 0.04	−1.52 ± 0.09	145 ± 18	3.44	0.94 ± 0.10	3.04 ± 0.09	...
990518	−0.52 ± 0.04	−1.45 ± 0.20	174 ± 22	2.07	0.93 ± 0.20	2.90 ± 0.20	(i)

Note.—For most events, the fluence interval is the same interval used in making the temporal fit. Uncertainties in the model parameters are taken from the covariance matrix.

[a] Here α and α' are the indices of the of the spectral energy flux, F_ν (in units of ergs s^{-1} cm^{-2} keV^{-1}), i.e., $\alpha = \alpha_{low} + 1$ and $\alpha' = \alpha_{high} + 1$.

[b] Characteristic signatures of the synchrotron spectrum as described in § 3.3 of the text.

[c] Within $1.5\,\sigma$.

[d] Note that the value of α is consistent with the spectral slope below ν_c in the fast-cooling mode and the spectral slope below ν_m in the slow-cooling mode. In the former case, p is undetermined. For slow cooling, $p = 2.18$.

a broken power-law (BPL) model is a better representation of the data (Preece et al. 1998). Spectra of X-ray afterglows in the 2–10 keV range observed with *BeppoSAX* are best fitted with a single power law, with spectral indices that range from −1.5 to −2.3 (Costa 2000). Recently, it has been noted that the breaks in the synchrotron spectrum may not be sharp but rather smooth (Granot & Sari 2002). Therefore, we chose two spectral forms to model the spectra of the gamma-ray tails: a single power law as a baseline function and a smoothly broken power law (SBPL). The SBPL was chosen to enable direct comparison with the spectral form of the synchrotron shock model.

Because we are interested in the spectral behavior during late times of the burst, the CONT data type from individual detectors is the optimum choice of available data types from the LADs. CONT affords the best compromise between temporal and energy coverage, with 16 energy channels and 2.048 s time resolution. Coarse temporal and energy bins are required since we are dealing with a signal that continuously decays with time.

We model the photon spectrum (in units of photons s^{-1} cm^2 keV^{-1}) using the standard deconvolution and the Levenberg-Marquardt nonlinear least-squares–fitting algorithm that incorporates model variances. The spectra were modeled using CONT channels 2–14, which covered the energy range of ∼30–1800 keV. Count spectra from the two brightest detectors (i.e., the two detectors with the smallest source angles to the LAD normal vector) were generally used to make the fits. In some cases, the source angles differed substantially (>20°), resulting in a normalization offset in the count spectra between the two detectors. The data from the two detectors were fitted jointly with a multiplica-

tive effective area correction term in the spectral model. For bursts in which the effective area correction was small ($\lesssim$5%), we summed the CONT count rates from the individual detectors to maximize the count statistics. These were cases in which the source angles of the two detectors differed by only a few degrees. Detectors with angles to the source exceeding 60° or with strong signal from sources such as Vela X-1 or Cyg X-1 were excluded from the fit.

The free parameters of the power-law spectral model are the amplitude and the power-law index α_p. The free parameters of the BPL and SBPL are the amplitude, low-energy index α_{low}, high-energy index α_{high}, and the break energy E_b. The slopes of the spectral energy flux F_ν are readily obtained from the simple relations $\alpha = \alpha_{low} + 1$ and $\alpha' = \alpha_{high} + 1$.

For the decay emission of each burst, we modeled the time-integrated spectrum defined over a time interval that was either the same as or shorter in length than the time interval used in making the temporal fits. In all cases, the time interval was restricted *to the region of the burst during the power-law decay*. Shorter time intervals were used for events with weaker signal-to-noise ratio (S/N). For the PF class bursts, however, we selected the entire burst emission (spectra of the burst intervals starting at the peak gave nearly identical parameter values). For the majority of events, the SBPL model was preferred over the single power-law model. Summarized in Table 2 are the spectral fit parameters for events where the SBPL was the better choice of model based on the χ^2 statistic. In six bursts, however, the fitted value of the high-energy slope was unusually steep ($\lesssim$ −4.0). Preece et al. (1998) pointed out that spectral models with curvature can sometimes overestimate the steepness

TABLE 3
Time-integrated Spectral Fits: Single Power Law

GRB	Trigger	α_p[a]	χ^2 / dof	p[b]
910602	257	-0.52 ± 0.01	1.05	1.04 ± 0.01
911016	907	-1.77 ± 0.22	1.22	3.54 ± 0.22
920813	1807	-1.01 ± 0.02	13.2	2.02 ± 0.02
930131	2151	-0.89 ± 0.11	0.89	1.78 ± 0.11
951104	3893	-1.47 ± 0.05	4.96	2.94 ± 0.05
970302	6111	-0.73 ± 0.10	1.13	1.46 ± 0.10
990322	7488	-0.42 ± 0.06	1.51	0.84 ± 0.06
990415	7520	-1.28 ± 0.16	1.19	2.56 ± 0.16
000103	7932	-1.99 ± 0.43	1.34	3.98 ± 0.43

Note.—For most events the fluence interval is the same interval used in making the temporal fit. Uncertainties in the model parameters are taken from the covariance matrix.

[a] The power-law index is the index of the spectral energy flux F_ν (in units of ergs s^{-1} cm^{-2} keV^{-1}).

[b] Here $p = -2\alpha_p$.

of the high-energy slope, depending on how well the data tolerate curvature (see Fig. 1 in Preece et al. 1998). The broken power-law model was therefore used for these six events, resulting in slightly better reduced χ^2-values and better constrained values of the fitted high-energy slope. This resulted in spectral parameters for a total of 20 bursts. The reduced χ^2-values are reasonable, although a few bursts for which joint fits were made tended to give slightly larger values (χ^2/dof $\gtrsim 2$). Given in the table are the fitted values of the spectral indices, the break energy, and their uncertainties from the covariance matrix. Also given are the difference in spectral slope across the break energy $\Delta = |\alpha' - \alpha|$ and the value of p calculated from the high-energy spectral slope.

Of the remaining bursts, nine events were best represented by the single power-law function. The best-fit parameters and the corresponding value of p are presented in Table 3. The spectral fits for the remaining 12 events resulted in poor χ^2-values and poorly constrained parameter values, regardless of the choice of spectral model. These are clearly cases when the counting statistics are too poor to constrain the model parameters and therefore were excluded. The results in Table 3 should be interpreted with some degree of caution. These events may be cases in which the flux level was to low, causing the break in the spectrum to be washed out in the counting noise. In such cases, the single power law will often be adequate to model the spectrum even though the true burst spectrum may contain a break.

A careful inspection of Table 2 immediately allows us to identify high-energy afterglow candidates based on three characteristic signatures of the synchrotron spectrum, which we categorize as the following: (1) in the fast-cooling mode, the spectral slope below the high-energy break (ν_m) is *always* $-\frac{1}{2}$ for radiative or adiabatic evolution, as seen from equations (3) and (4), (2) in the slow-cooling mode, the change in spectral slope across the high-energy break (ν_c) is *always* $\frac{1}{2}$, as seen from equation (5), and (3) the electron energy index p calculated from the measured spectral slope should have a value in the range $2.0 \leq p \leq 2.5$, the typical range derived from afterglows observed at X-ray, optical, and radio wavelengths.

Applying these criteria, we label events with these properties in the last column of Table 2. We thus immediately iden-

tify several fast-cooling candidates: GRB 920622, GRB 940419b, GRB 960530(2), and GRB 980301. Each of these events has a value of α within 1 σ of -0.5 and a value of p similar to those found for afterglows. GRB 970411, GRB 971208, GRB 990316, and GRB 990518 are only marginally consistent with fast cooling, having larger p-values and reduced χ^2-values. None of the events in Table 2 are consistent (within 1 σ) with $\Delta = 0.5$, suggesting no slow-cooling candidates (however, five events [GRB 920218, GRB 920622, GRB 920801, GRB 940419b, and GRB 980301] have values within 2 σ). A total of nine bursts in Table 2 are ruled out as high-energy afterglow candidates because their spectral parameters bear no resemblance to the fast-or slow-cooling synchrotron spectrum. One event of notable interest is GRB 981203, which has α- and α'-values consistent with a cooling break ν_c, as opposed to ν_m in the fast-cooling spectrum. This implies a ν_m break above ~ 2 MeV, while the value of p remains unconstrained by the data. In § 4 the early high-energy afterglow candidates are discussed in greater detail.

Obviously, for the single power-law events listed in Table 3, we have less spectral information. The value of p given in Table 3 is derived from α_p under the assumption that α_p is the slope above the break for fast or slow cooling. Clearly, this need not be the case. A case in point is GRB 910602, which has $\alpha_p = -0.52 \pm 0.01$, a value consistent with the spectral slope of fast cooling for $\nu_c < \nu < \nu_m$. In this interpretation the cooling break ν_c would be below the BATSE window and ν_m above. The value of p would be undetermined from the data. Scanning the values of p given in Table 3, we find $p = 2.56 \pm 0.16$ for GRB 990415, a typical value for afterglows. This suggests that the measured slope $\alpha_p = -1.28 \pm 0.16$ could be the slow- or fast-cooling high-energy slope. What values of the spectral slope do we expect to observe below ν_c for slow cooling? If we assume a value of $p = 2.5$, then the calculated slope below ν_c is $\alpha = -(p-1)/2 = -0.75$. We find one burst, GRB 970302, with $\alpha_p = -0.73 \pm 0.10$, consistent with the expected value if $p = 2.5$.

An additional constraint we can apply to the data is a comparison of the measured temporal slopes with their expected values derived from the measured spectral indices given in the expressions in equation (6). A plot of the temporal versus spectral index for the data in Table 2 is shown in Figure 3. Here the spectral index is the high-energy spectral energy index α' in the fourth column of Table 3. For comparison with the models, we plot the possible linear relationships between α' and β given in equation (6). Note that this plot should be interpreted with a certain degree of caution. The expected values of α' are somewhat restricted by the possible range of p-values between 2.0 and 2.5 predicted by Fermi acceleration models (see, e.g., Gallant, Achterberg, & Kirk 1999; Gallant et al. 2000). Interestingly, however, five events (*filled diamonds*) are consistent with the $\beta = -p$ line for adiabatic jet evolution. We address this implication in detail in §§ 4 and 5.

A similar plot is shown in Figure 4 for the single power-law fits from Table 3. In general, all but one event appear consistent with the relations between the temporal and spectral indices expected from external shocks. Thus, closer inspection of the spectral parameters (e.g., α_p and p) in Table 3 is required to establish if these are viable high-energy afterglow candidates (see § 4).
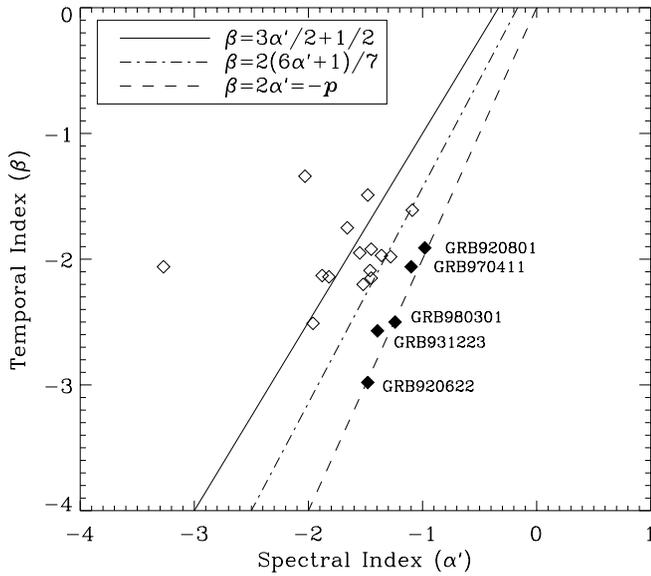
FIG. 3.—Plot of high-energy spectral index vs. temporal index for the 20 events listed in Table 2. Also plotted are the linear relationships expected from the evolution of an adiabatic spherical blast wave (*solid line, dot-dashed line*) and a jet (*dashed line*). The five bursts labeled on the plot (*filled diamonds*) are within 1 σ of the $\beta = 2\alpha'$ line.
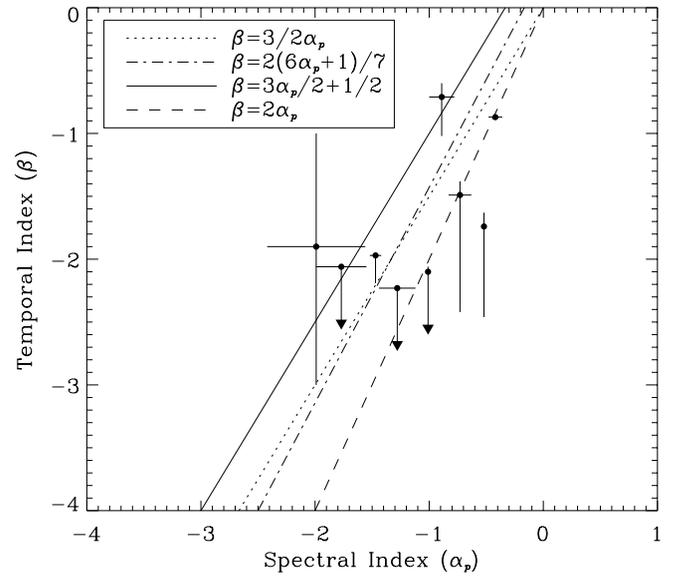

FIG. 4.—Plot of spectral index vs. temporal index for the nine events listed in Table 3. The asymmetric uncertainties in the temporal indices reflect the 68% joint confidence intervals between β and t_0. Thus, the uncertainties for bursts with highly elongated $\Delta\chi^2$ contours are indicated by downward arrows. Lines indicate the linear relationships expected in the synchrotron afterglow spectrum: $\nu_m < \nu < \nu_c$ in slow cooling, $\beta = 3\alpha_p/2$ (*dotted line*), $\nu_m < \nu$ in adiabatic fast cooling or $\nu_c < \nu$ in slow cooling, $\beta = 3\alpha_p/2 + \frac{1}{2}$ (*solid line*), and for $\nu_m < \nu$ in radiative fast cooling, $\beta = 2(6\alpha_p + 1)/7$ (*dot-dashed line*). Also plotted is the $\beta = 2\alpha_p$ line for adiabatic jet evolution. Since we do not observe a break in the spectrum for these events and thus cannot distinguish if the observed power-law index is the low or high-energy index, we plot all possible relationships between the spectral and temporal index.

3.4. *Spectral Evolution: Color-Color Diagrams*

The evolution of the synchrotron spectrum is unique for a given hydrodynamical evolution of the blast wave. This evolution can be traced in a graphical form using a CCD. The CCD method is a model-independent technique that characterizes the spectral evolution of the burst over a specified energy range. With this method, a comparison of spectral evolution patterns among GRBs can be made in addition to a comparison with patterns expected from the evolution of the synchrotron spectrum.

The CCD is a plot of the hard color versus the soft color, where the hard and soft colors are defined as the hardness ratios (i.e., ratios of the count rates) between (100–300/50–100 keV) and (50–100/25–50 keV), respectively. To construct the CCDs, we use the count rates in the three lowest (25–300 keV) of the four broad energy channels from the DISCSC data. We select a time interval large enough to cover most of the burst emission until the statistical noise begins to dominate. These bins are identified by hardness ratios with 2 σ upper limits. We also fold the fast- and slow-cooling broken power-law synchrotron spectra of a spherical blast wave through the LAD detector response to obtain the expected count spectrum (dashed and solid lines, respectively, in Figs. 5–8). We assume that the fast-cooling spectrum is radiative, with $p = 2.4$, and that $\alpha_{\rm low} = -1.5$, and we allow E_m to evolve from 220 to 25 keV. For the slow-cooling spectrum, we also assume $p = 2.4$ and the same evolution for E_c.

Giblin et al. (1999b) have shown that the tail emission from GRB 980923 resembles that of afterglow synchrotron emission due to an external shock. To illustrate the usefulness of the CCD technique, we show in Figure 5 the CCD for GRB 980923. In this representation, the time evolution of the burst is preserved by a color sequence of the hardness ratios, with black/violet/blue signaling the onset of the burst and yellow/red signaling the end of the burst. The left-hand panel shows the CCD for the time interval that

brackets the entire burst (variability + tail). The variable emission of the burst shows a crescent-like pattern decoupled from a cluster of points that represent the tail of the burst. The crescent pattern is typical among GRBs (Kouveliotou et al. 1993b; Giblin et al. 1999a); however, the clustering is less common. The crescent track exhibits a saw-toothing of soft-hard-soft evolution, indicative of the spectral behavior of the individual pulses that comprise the main burst emission. The pattern drastically changes when the variability ceases and the tail becomes visible. The tail cluster overlaps the region of the two-color plane that contains the evolution of the slow- and fast-cooling synchrotron spectrum. This is best illustrated in the right-hand panel of Figure 5, where the CCD is constructed from a longer time interval in the tail only. Unfortunately the CCD pattern of the tail is not completely resolved because of the increasingly large uncertainties in the hardness ratios that arise from the decreasing flux level. However, the points do lie in the correct region of the diagram. This decoupling of the points in the model-independent CCD is clear evidence for two distinct spectral components observed in a GRB .

Figure 6 shows the CCDs for the four fast-cooling candidates identified based on their spectral parameters in Table 2. The pattern for GRB 920622 bears a striking resemblance to that of GRB 980923 in the left-hand panel of Figure 5. Like GRB 980923, this burst contains a period of variability followed by a very smooth emission tail. The crescent pattern that arises from the variable part of the burst is clearly visible and spans nearly the same range of soft and hard color indices. However,
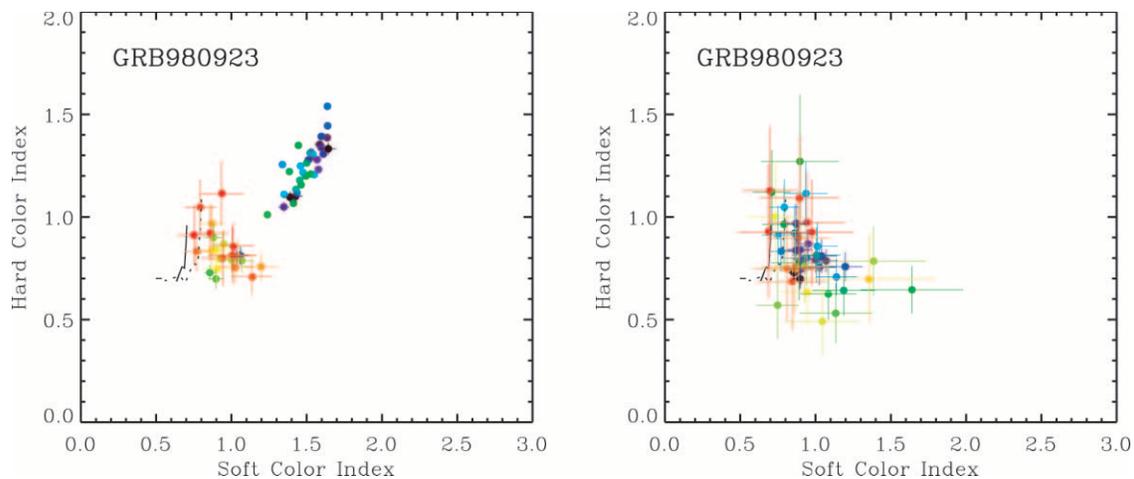
Fig. 5.—*Left*: Color-color diagram of GRB 980923 variability episode *and* tail emission (0–70 s). The crescent-like pattern is the variable emission, while the decoupled cluster of points is the tail emission. *Right*: Color-color diagram of the tail emission only, covering a much longer time interval (40–100 s). Also plotted are the evolution patterns expected from the slow (*solid line*) and fast-cooling (*dashed line*) synchrotron spectrum.

the clear discontinuity between the burst emission and the tail emission in the CCD of GRB 980923 is not as pronounced in the CCD of GRB 920622. Nonetheless, the tail emission (*orange and red points*) lies in the same region as those of GRB 980923 and the synchrotron afterglow spectrum. The CCD pattern for GRB 949419b

(in the PF class) is similar but appears more cluster-like in the region of synchrotron evolution.

Another burst of interest in the PF category is GRB 960530. This event consists of two FREDs separated by ~200 s. The second FRED only has about half of the peak intensity as the first. The CCD for the second FRED is seen
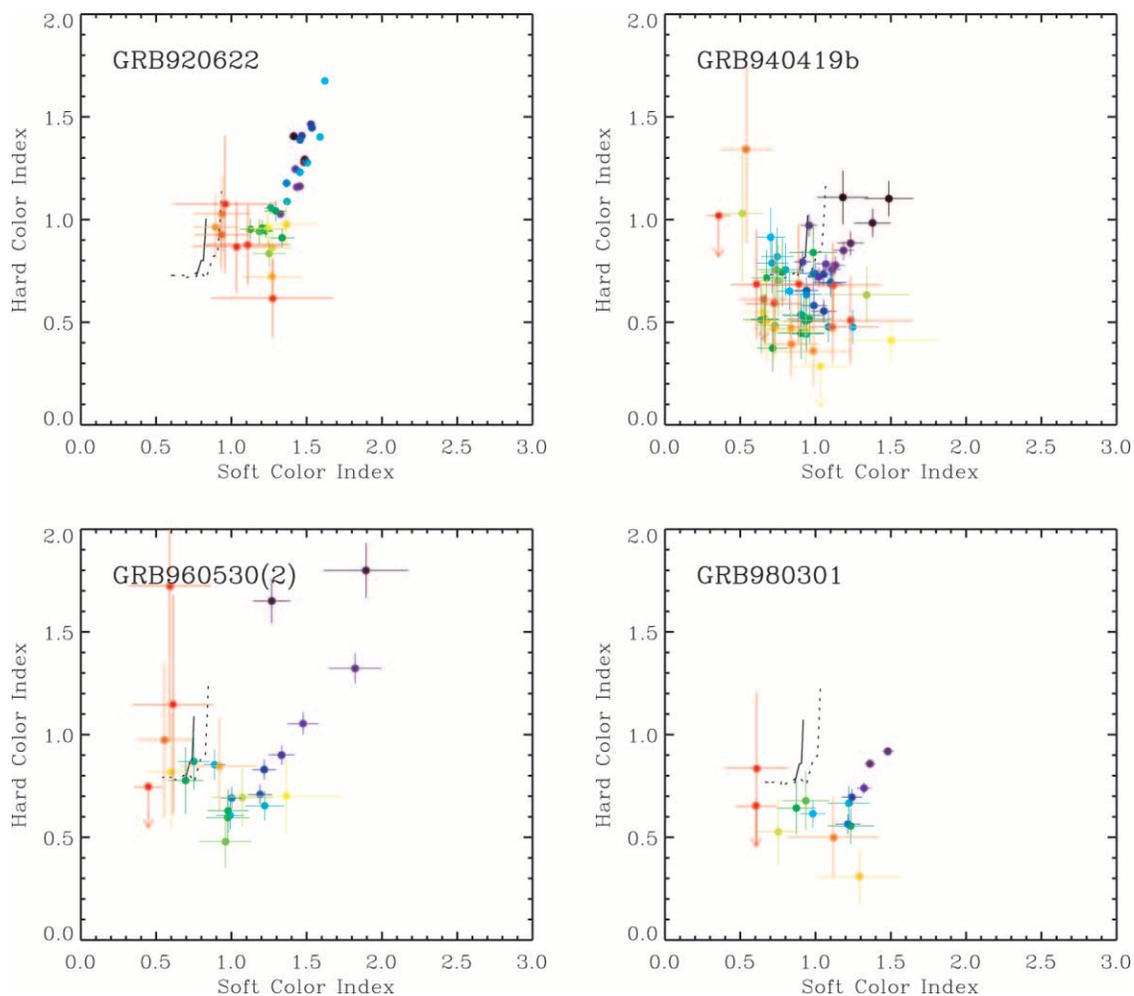

Fig. 6.—Color-color diagrams for the four fast-cooling candidates from Table 3. Arrows indicate 2 σ upper limits.
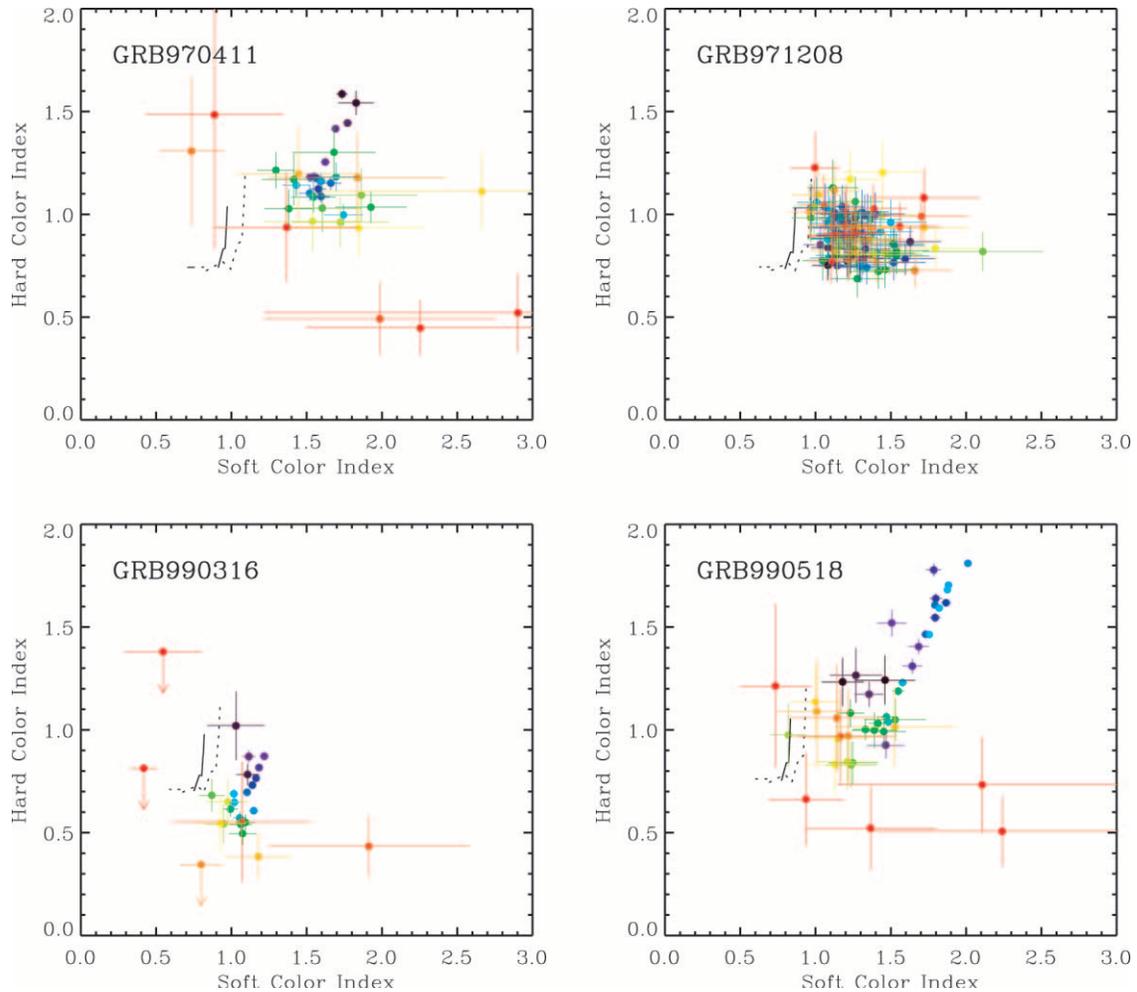
FIG. 7.—Color-color diagrams for the marginal fast-cooling candidates from Table 3. Arrows indicate 1 σ upper limits.

in Figure 6. The episode begins very hard on the rise and evolves through the synchrotron spectrum during the decay. Interestingly, although the first episode of GRB 960530 is also a FRED, its color-color diagram (Fig. 8) shows a broad crescent pattern that evolves much farther away from the synchrotron pattern. This may be a case where the external shock is clearly decoupled in time from the GRB .

The last event in Figure 6, GRB 980301, shows an intriguing pattern that closely resembles the evolution pattern of the synchrotron spectrum. The evolution is mainly shaped like a reverse "L" but marginally offset to higher soft color values and lower hard color values. In this case it is difficult to argue in favor or against the synchrotron model.

Figure 7 shows the CCDs of the four events from Table 3 that are only marginally consistent with fast cooling. GRB 970411 and GRB 990518 show similar patterns that resemble those in Figure 6, but the consistency with the synchrotron pattern is weak. GRB 971208 shows little evolution and a cluster of points partially overlapping the synchrotron region. GRB 990316 shows a nearly identical pattern to that of GRB 980301.

A total of 23 events from our sample showed CCDs inconsistent with the evolution of the synchrotron spectrum. Rather, most of these events showed the crescent pattern that are common among GRBs, as depicted in Figure 8. These events span a much larger range of hard and

soft colors than expected from the synchrotron emission alone. Others were too weak to distinguish a pattern.

4. HIGH-ENERGY AFTERGLOW CANDIDATES

We identify a total of eight events from our sample of 40 as high-energy afterglow candidates based on their observed spectral parameters and color-color diagrams. Each burst is discussed in detail below.

4.1. *GRB 910602*

The observed spectral slope for GRB 910602 is consistent with the spectral slope below ν_m in the fast-cooling spectrum, although the slope below ν_c in slow cooling cannot be ruled out, implying a value of $p = 2$. A series of time-resolved fits with a uniform time resolution of 4.096 s revealed no softening of the spectrum; i.e., the slope remained constant with $\alpha_p \sim -0.5$ throughout the tail. Applying the relations in equation (6) for slow cooling, we expect $\beta = -0.78 \pm 0.01$ and, from equations (4) and (5), for fast cooling we expect $\beta = -\frac{4}{7}$ (radiative) or $\beta = -\frac{1}{4}$ (adiabatic). These values do not agree with the measured value $\beta = -1.74^{-0.72}_{+0.11}$. Although the spectrum appears to be consistent with that of the synchrotron spectrum, the evolution does not appear to be consistent with the evolution of a spherical blast wave.
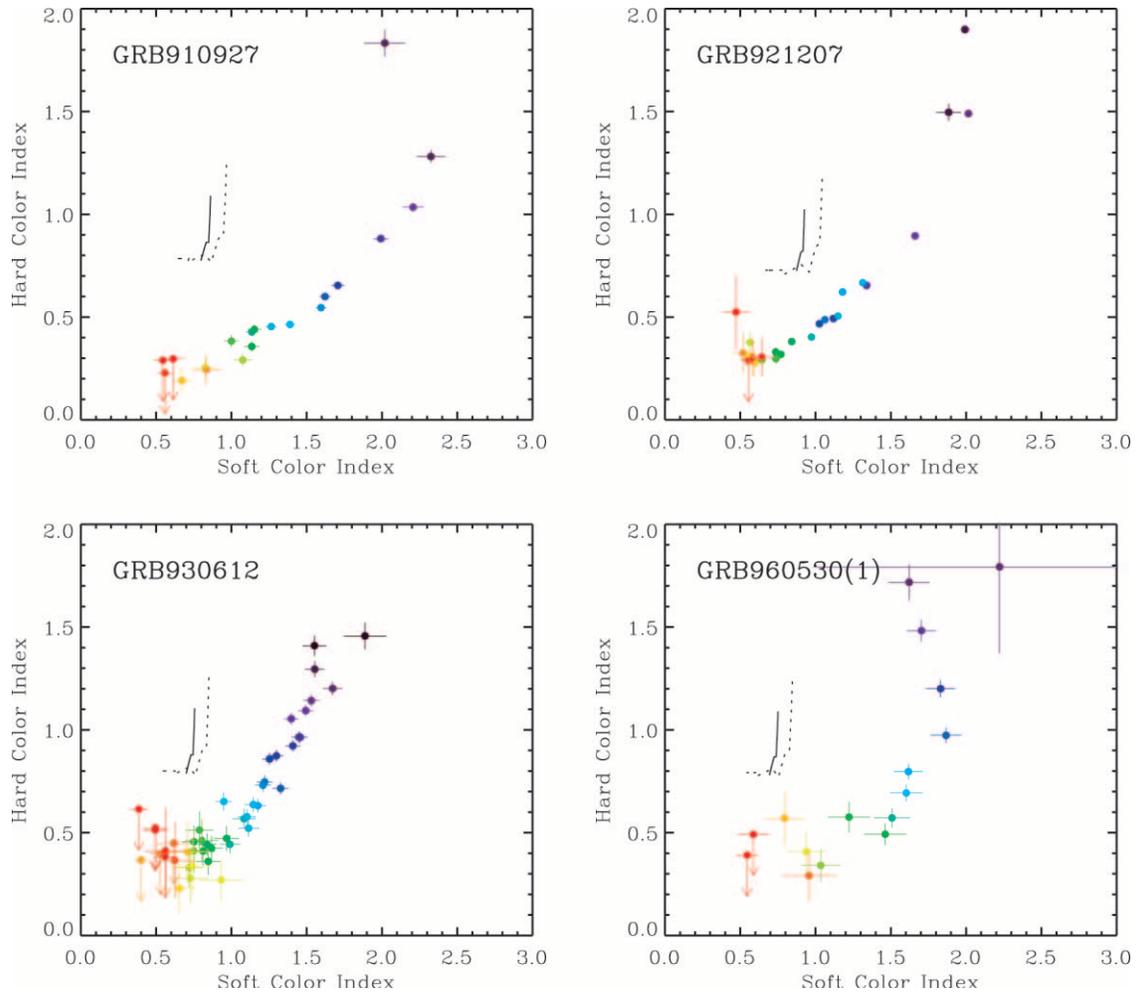
Fig. 8.—Sample of color-color diagrams of GRBs that are not consistent with the evolution of the synchrotron spectrum. Arrows indicate 2σ upper limits.

4.2. GRB 920622

The time history of this burst bears a striking resemblance to that of GRB 980923 reported by Giblin et al. (1999b). Initially, the burst is highly variable, then at ~ 18 s after the trigger time the burst enters a phase of smooth decay that lasts until ~ 50 s after the trigger. From Table 2, the time-integrated spectral fit suggests fast cooling, with low-energy index $\alpha = -0.49 \pm 0.04$. From the high-energy index, a value of $p = 2.96 \pm 0.26$ is inferred. The value of $\Delta = 0.99 \pm 0.26$ is marginally consistent (within 2σ) with the expected value of 0.5 for slow cooling. The time-integrated spectrum of the variable emission of the burst is in contrast with the fluence spectrum of the tail. The variable emission gives $\alpha_v = -0.07 \pm 0.01$, $\alpha'_v = -1.50 \pm 0.04$, and $E_{v,b} = 370 \pm 12$ keV, suggestive of a spectral change near ~ 18 s. Note that the spectral parameters of the variable emission are *not* consistent with the synchrotron spectrum. We binned the tail emission into three time bins with $S/N \geq 45$ to model the spectral evolution; however, the parameters were poorly constrained because of the steep nature of the flux decay. The spectral evolution of the variability + tail emission, however, can be seen in Figure 6. The tail of the burst appears consistent with the region of the diagram defined by the evolution of the synchrotron spectrum. The measured temporal index of the tail is $\beta \leq -2.98$,

clearly inconsistent with the expected values for β for $\nu < \nu_m$. Interestingly, however, β is nearly identical to the value of p inferred from the high-energy slope, as expected for jet evolution.

4.3. GRB 940419b

The smooth rise and decay structure of this burst places it in the PF category. Like the tail emission of GRB 920622, this burst also shows a low-energy slope consistent with the fast-cooling spectral slope below ν_m. The measured temporal slope is $\beta \leq -1.75$. While this slope is not consistent with the temporal index below ν_m, it is consistent with the expected values of $\beta = -2.56 \pm 0.55$ (radiative) and $\beta = -1.95 \pm 0.55$ (adiabatic) for $\nu > \nu_m$, given the large uncertainties. We further binned the data in the tail to $S/N \geq 45$ and constrained the evolution of the break energy by holding the low- and high-energy spectral indices fixed to their values derived from the time-integrated fit. We find $E_b \sim (t - t_0)^{-1.21 \pm 0.15}$ for t_0 fixed at -25.0 s (χ^2/degrees of freedom [dof] $= 7.52/8$). Additional fits with other larger values of t_0 gave slightly shallower indices, as expected if one compares the behavior to that of β and t_0. For an adiabatic fast-cooling spherical blast wave, we expect the break energy to decay as -1.5, within 2σ of our measured value. As seen from the CCD in Figure 5, the

spectral evolution of this burst is very close to that of the synchrotron spectrum, although the rise of the burst tends to be somewhat harder in the soft color index than expected from evolution of the synchrotron spectrum alone.

4.4. GRB 960530

GRB 960530 is of particular interest because of its striking temporal behavior. The burst has two distinct episodes of emission, each having a FRED-like time profile. The second episode, much weaker with a peak intensity less than half of the first, occurs ~ 200 s after the first. As seen in Table 2, the low-energy slope of the second episode is consistent with the fast-cooling slope below ν_m; however, the value of $p = 3.76 \pm 0.37$ is large mainly because the high-energy slope is not well constrained. The value of p derived for the first episode is not unreasonable; however, the low-energy slope is roughly 3σ away from the expected value of -0.5. The decay index for the second episode is $\beta \le -2.13$, not inconsistent with the expected values $\beta = -4.57 \pm 1.57$ and $\beta = -3.75 \pm 1.57$ for radiative and adiabatic fast cooling, respectively. The CCD of the second emission episode of this burst (Fig. 6) indicates that during the decay the emission evolves into the synchrotron spectrum.

4.5. GRB 970411

From Table 2, the low-energy index of this burst is nearly 4σ from the value -0.5 expected in the fast-cooling regime. However, it does have $p = 2.2 \pm 0.08$, consistent with typical afterglow values and particle acceleration models of relativistic shocks (see, e.g., Gallant et al. 2000). Additionally, the change in slope Δ is less than 3σ from the expected value of -0.5 for the cooling break in the slow-cooling regime. For slow cooling, we expect the temporal slope to be $\beta = -0.53 \pm 0.04$ for $\nu < \nu_c$ and $\beta = -1.15 \pm 0.08$ for $\nu > \nu_c$. For $\nu > \nu_m$ in fast cooling we expect $\beta = -1.60 \pm 0.08$ (radiative) and $\beta = -1.15 \pm 0.08$ (adiabatic). Our measured value of the decay, $\beta = -2.06^{-0.21}_{+0.20}$, is marginally consistent (within 2σ) with the radiative fast-cooling slope. More notably, it is consistent (within 1σ) with the value of p. A series of spectral fits during the tail of the burst holding the low- and high-energy spectral indices constant show that E_b decays with time described by a power law of the form $E_b \sim (t - t_0)^{-0.96 \pm 0.26}$ for $t_0 = 16$ s ($\chi^2/\mathrm{dof} = 4.02/3$), marginally consistent with the adiabatic evolution (spherical or jet) of ν_m.

4.6. GRB 971208

GRB 971208 is the longest burst ever detected with BATSE. The temporal structure of the burst is a simple smooth FRED lasting several thousand seconds. The emission is soft, with no emission in channel 4 ($E > 300$ keV). The spectral parameters tend to favor fast cooling, but not strongly, since the value of $p = 4.06 \pm 0.04$ is unusually high. The value of $\Delta = 1.48 \pm 0.04$ is well determined and very far from the value expected for slow cooling ($\Delta = 0.5$). Although in apparent contradiction to this, the CCD pattern for this event (Fig. 7) shows a strong resemblance to that of the tail of GRB 9890923 in Figure 5.

4.7. GRB 980301

GRB 980301 shows a low-energy slope consistent with fast cooling but also a value of $p = 2.48 \pm 0.13$, remarkably consistent with values of observed afterglows. The change

in slope across the break energy is slightly higher than that expected for slow cooling (but within 2σ). If the spectrum is fast cooling, then we expect $\Delta = 0.74 \pm 0.13$, based on the measured high-energy slope. This value is within 1σ of the value $\Delta = 0.69 \pm 0.13$ that we derive from the measured slopes. For radiative evolution, we expect $\beta = -1.84 \pm 0.13$, while for adiabatic evolution, we expect $\beta = -1.36 \pm 0.13$. However, we measure a much steeper value of $\beta = -2.50^{-1.58}_{+0.05}$, suggesting an evolution inconsistent with the hydrodynamics of a spherical blast wave but consistent with that of a jet. The CCD pattern for GRB 980301 is shown in Figure 6. Although very similar to the model pattern, the observed pattern appears to be displaced.

4.8. GRB 981203

The measured low- and high-energy spectral indices for this event are notably different than those of other bursts listed in Table 2. The low-energy spectral index is consistent with the spectral slope below ν_m in the slow-cooling mode and below ν_c in the *fast-cooling* regime. Interestingly, for the *fast-cooling* regime the high-energy index is marginally consistent with the spectral slope for $\nu_c < \nu < \nu_m$. The direct implication here is that ν_m is above the BATSE window and has yet to evolve through. Hence, the value of p is undetermined. The flux in the tail was too weak to follow the evolution of the spectrum with any reasonable accuracy. From equations (3) and (4), clearly the temporal decay should be very shallow, unlike our measured value of $\beta = -1.61^{-0.013}_{+0.002}$. This evolution is not consistent with the evolution of a spherical blast wave into a constant density medium.

5. DISCUSSION

The diverse temporal and spectral properties of GRBs leave their origin open to different interpretations. From our analysis, we have identified a subset of gamma-ray bursts that exhibit smooth high-energy (~ 25–300 keV) decay emission whose spectral properties are very similar to that of fast-cooling synchrotron emission that results from a power-law distribution of relativistic electrons accelerated in a forward external shock. The 25–300 keV time histories of the high-energy afterglow candidates are shown in Figure 9. The diversity of the time profiles suggests that the GRB time history is *not* necessarily the distinguishing feature of external shock emission in the fireball model. The diversity also suggests that the afterglow may be disconnected from the burst emission (e.g., GRB 960530) or overlap the burst emission (e.g., GRB 920622). *BeppoSAX* has demonstrated the existence of both cases: overlap or continuation of the afterglow onset with the prompt burst emission (e.g., GRB 970508 [Piro et al. 1998] and more recently GRB 990510 [Pian et al. 2001]) and the case in which the afterglow begins at a later time, disconnected from the prompt GRB (e.g., GRB 970228 [Costa 2000]). Our analysis further suggests that in some cases (e.g., GRB 971208) the early high-energy afterglow may actually be the burst emission itself. This situation could arise if the energy deposition in the internal shocks is too low.

The spectra of a significant fraction of bursts in our sample, however, show inconsistencies with the synchrotron model. From a catalog of BATSE GRB spectra, we see that the low- and high-energy spectral indices follow well-
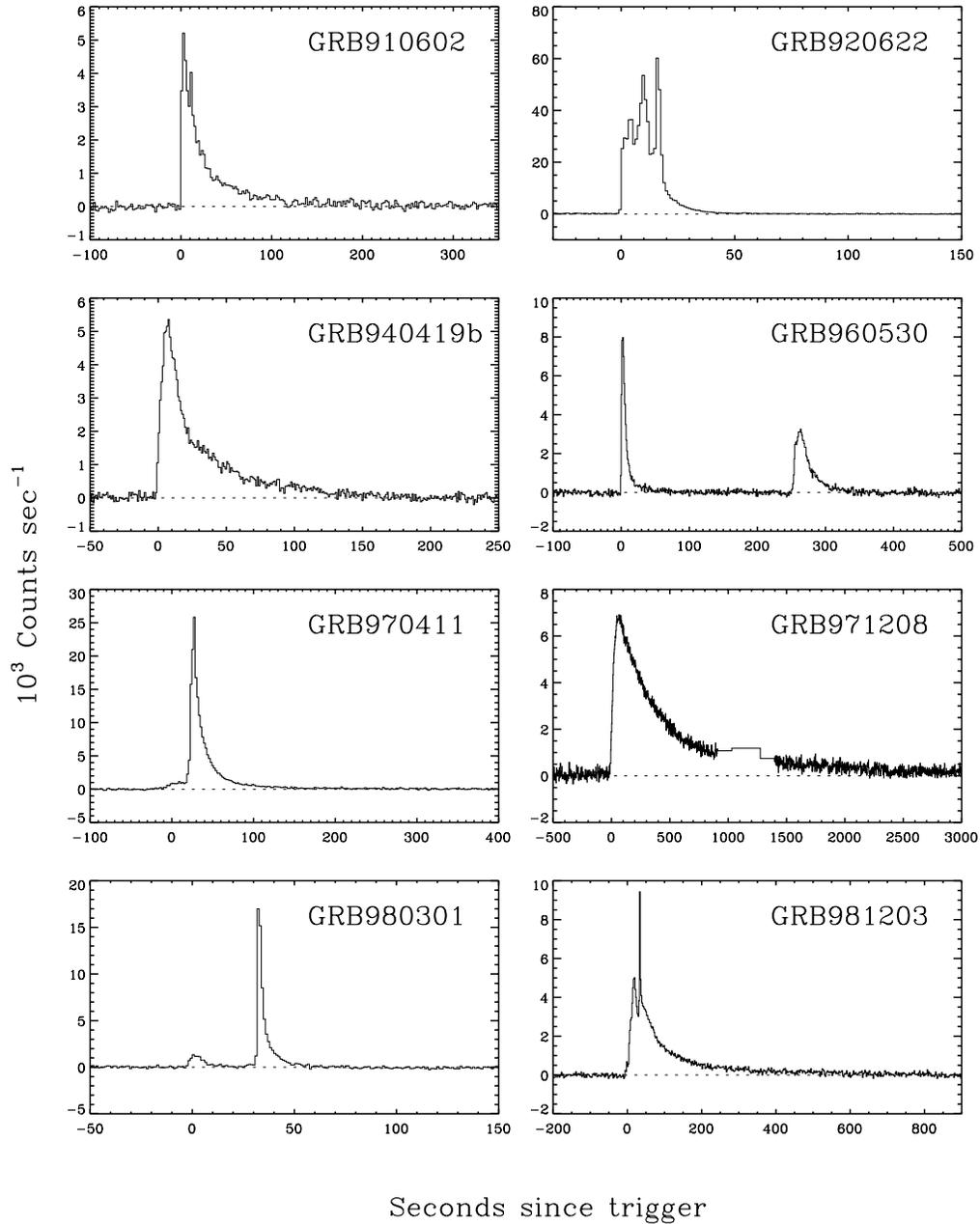
FIG. 9.—Time histories (25–300 keV) for the eight high-energy afterglow candidates

defined distributions (Preece et al. 2000). For example, the distribution of low-energy power-law indices given in Figure 7 of Preece et al. (2000) peaks near $\alpha_{low} \sim -1$. Roughly 200 of the 5500 spectra in the distribution are consistent with the expected value of α_{low} below ν_m, or about $\sim 4\%$. If we adopt the hypothesis that GRB spectra are *not* synchrotron spectra, then on average $\sim 4\%$ of the time we expect to measure parameters consistent with the synchrotron spectrum purely by chance coincidence. This implies that we can expect ~ 0.8 events from Table 2 to have $\alpha_{low} = -1.5$ ($\alpha = -0.5$) purely by chance. Clearly, our total of eight candidate events exceeds this limit. These events are thus likely sources of synchrotron emission.

Recent studies on electron acceleration models for ultra-relativistic shocks predict values of the electron index in a narrow range $2.0 \leq p \leq 2.5$ (Gallant et al. 1999, 2000). Our

values maintain a significant dispersion under the assumption that the observed high-energy afterglow is equivalent to the high-energy slope of the fast- *or* slow-cooling synchrotron spectrum (i.e., $\alpha_{high} + 1 = -p/2$). Electron indices in Table 2 tend to be steeper on average than $p = 2.5$. One possible alternative for a high value of p ($p \simeq 3$) may be due to a shock generated in a decreasing density, $n \propto r^{-2}$, external medium that is the result of a massive stellar wind (Chevalier 1998; Chevalier & Li 1999). On the other hand, Sari (2000) pointed out that there is no reason why the value of p should be different for wind models. Note that several values of p in Table 3 are *below* $p = 2$. Hard electron indices ($1 < p < 2$) have recently been reported for the jet model of GRB 00301c (Panaitescu 2001) assuming a broken power-law electron energy distribution. Similarly, a jet interpretation for GRB 010222 would also require a flatter electron

index, based on analysis of the *BeppoSAX* data (in't Zand et al. 2001). However, in't Zand et al. (2001) show that the slowing of the ejecta into the nonrelativistic regime yields $p = 2.2$. From a theory viewpoint, Malkov (1999) has shown that it is possible to obtain a hard electron distribution in Fermi acceleration models. While the model predictions for the range of electron indices appear somewhat uncertain, the *observed* dispersion in p-values may be strongly linked to the accuracy of the fitted value of α_{high}. Systematic effects may play a role that introduces a bias toward steeper values in the estimation of the high-energy power-law index.

Our analysis shows that the tail temporal decays are well-described by a power law with a mean index $\langle \beta \rangle = -2.03 \pm 0.51$. While the spectral parameters of approximately 20% of the decays in our sample are in generally good agreement with the synchrotron spectrum, the temporal evolution, in general, does not agree well with the evolution of a spherical blast wave in a homogeneous medium. There are alternatives that might explain this deviation: First, we only considered fully radiative or fully adiabatic evolution. More than likely the fireball is neither fully radiative nor fully adiabatic throughout its evolution, although at the very early stages the evolution may nearly be fully radiative while at latter stages the evolution is completely adiabatic. Böttcher & Dermer (2000) have considered the early afterglow regime with the intermediate cases: partially radiative or partially adiabatic blast waves. They find that the temporal decay of the spectral flux in the fast-cooling regime is a function of $\epsilon = \epsilon_e \epsilon_{rad}$, where ϵ_{rad} is the fraction of energy radiated by the accelerated electrons, or $F_\nu \propto \nu^{-1/2} t^{-2[(1+\epsilon)/(8-\epsilon)]}$ for $\nu_c < \nu < \nu_m$ and $F_\nu \propto \nu^{-p/2} t^{-\{[2(1+\epsilon)+6(p-1)]/(8-\epsilon)\}}$ for $\nu > \nu_m$. Higher efficiencies therefore produce steeper temporal slopes. However, as can be seen for $\epsilon = 0.8$, we obtain $F_\nu \propto \nu^{-1/2} t^{-1/2}$ for $\nu_c < \nu < \nu_m$. This is steeper than the expected value of $-\frac{1}{4}$ from equation (4) but not steep enough to match the discrepancies in our observations.

Another possibility to consider is a jetlike geometry or collimated outflow as opposed to the simple spherical blast wave. The break in the light curve may occur at early times after the initial shock, as in the case of GRB 980519, where evidence exists for a break to a steep decay that apparently occurred during the few hours between the GRB and the first afterglow detection (Sari et al. 1999). Rhoads (1999) has shown for adiabatic evolution that the time of the break in the observer's frame goes as $t_b \propto \theta_c^2$. A very early break therefore requires a very small θ_c. If $\theta_c < \theta_b$ initially, then the slope is steep from the start. This implies one of two possibilities: (1) very narrow emission spots, or "nuggets," within a narrow collimation angle or (2) a very small value of Γ such that $\Gamma^{-1} > \theta_c$. The second option is not likely since the observed emission is in the keV to MeV range and $\nu_m \propto \Gamma^4$, requiring a high Lorentz factor. A list of events from Tables 2 and 3 with comparable electron indices and temporal indices (as required for a jetlike blast wave) are presented in Table 4. Note that although the value of p for GRB 990322 is low, the temporal decay does follow the t^{-p} relation. Events with values of β shallower than p may be events in which the break occurs at some later time after the GRB . We categorize these events as prebreak jet candidates. Three of these events (GRB 940419b, GRB 960530, and GRB 970925) have some spectral properties characteristic of the synchrotron spectrum (see last column of Table

TABLE 4
JET CANDIDATES

GRB	Trigger	p	β
910602	257	2.00 ± 0.01^a	$1.74^{+0.72}_{-0.11}$
920622	1663	2.96 ± 0.26	> 2.98
920813	1807	2.02 ± 0.02	$2.10^{+6.05}_{-0.04}$
970302	6111	1.46 ± 0.10	$1.49^{+0.93}_{-0.11}$
970411	6168	2.20 ± 0.08	$2.06^{+0.21}_{-0.20}$
980301	6621	2.48 ± 0.13	$2.50^{+1.58}_{-0.05}$
990316	7475	3.04 ± 0.09	> 2.20
990322	7488	0.84 ± 0.06	$0.87^{+0.02}_{-0.01}$
990415	7520	2.56 ± 0.16	> 2.23
Prebreak Jet Candidates			
910131	2151	1.78 ± 0.11	$0.71^{+0.31}_{-0.11}$
940419b	2939	3.32 ± 0.55	> 1.75
960530	5478^b	2.96 ± 0.22	$1.49^{+0.77}_{-0.04}$
970925	6397	2.56 ± 0.13	$1.98^{+0.31}_{-0.21}$
971208	6526	4.06 ± 0.04	$1.34^{+0.11}_{-0.01}$

[a] This value assumes the spectrum is slow-cooling.
[b] First emissions episode of GRB 960530.

2). The five bursts labeled in Figure 3 are also candidates for jet outflows. More importantly, note that three of these events (GRB 920622, GRB 980301, and GRB 970411) are strong candidates because they belong to the group of high-energy afterglow candidates presented in § 4 that were selected based on their spectral properties. The spectra of the remaining two events (GRB 920801 and GRB 931223) are only marginally consistent with synchrotron emission from an external shock.

6. SUMMARY AND CONCLUSION

Our temporal and spectral analysis of the smooth extended gamma-ray decay emission in GRBs has shown evidence of signatures for early high-energy afterglow emission in gamma-ray bursts. The extended decay emission is best described with a power-law function $F_\nu \propto t^\beta$ rather than an exponential, similar to the results of Ryde & Svensson (2002), who studied the decay phase of a sample of GRB pulses with a broad range of durations. From our sample of 40 events, we find $\langle \beta \rangle \approx -2$ for long, smooth decays. Color-color diagrams have provided a qualitative interpretation of the burst spectral evolution and allow a simple comparison with the evolution expected from the synchrotron model as well as comparison of spectral evolution among GRBs. The CCD patterns and the spectral analysis indicate that $\sim$20% of the events in our sample are consistent with synchrotron emission expected from an external shock. Interestingly, three of these events have decay rates consistent with that expected from the evolution of a jet, $F_\nu \sim t^{-p}$. Because the break is essentially at the onset of deceleration, the jet must at least be very narrow since $\theta_c < 1/\Gamma$. Table 4 suggests that in some cases the break occurs at a later time, so that the prompt emission we observe is prebreak, $\theta_c > 1/\Gamma$, and consistent with spherical geometry. A possible scenario is one in which the ejecta is very grainy, where the nuggets in the ejecta are smaller than $1/\Gamma$, similar to the model discussed by Heinz & Begelman (1999). Huang et al. (1999; see also Wei & Lu 2000) have shown that the break in the light curve is more of a smooth transition due to the off-axis emission of a jet with no angu-

lar dependence. The steep light curve can only occur if the angular size of the nugget is less than $1/\Gamma$.

Connaughton (2002) has investigated the average late-time temporal properties of GRBs observed with BATSE and found statistically significant late-time power-law decay emission that softens relative to the initial burst emission, suggesting the existence of early high-energy afterglow. Other studies using PHEBUS (Tkachenko et al. 2000) and APEX (Litvine, Mitrofanov, & Koseyrev 2000) bursts show similar behaviors in late-time GRB light curves. Collectively, these studies strongly suggest that the afterglow emission may overlap or be connected to the prompt, variable burst emission. On the other hand, it is clear that not all GRBs exhibit such behavior. In some cases, the initial gamma-ray flux from the external shock may simply be too low to detect (see, e.g., Fig. 4 in Giblin et al. 2000). In other cases, the bulk Lorentz factor may be too low to generate the gamma-ray photons on impact with the surrounding medium.

As the number of afterglow/counterpart detections increases, the relationship of the afterglow emission to the gamma rays released in the initial phase of the burst can be studied systematically. The capabilities of *Swift* (Gehrels 2002) will allow broad spectral coverage using three co-aligned instruments (BAT, XRT, and UVOT) during the gamma-ray phase and early afterglow phase of the burst and facilitate the distinction between the GRB and the onset of the afterglow based on temporal *and* spectral information. With well-constrained spectral and temporal parameters in hand, plots of temporal index versus spectral index can be readily constructed and thus provide information on the geometry of the fireball and definitively test the internal/external shock model for GRBs.

REFERENCES

Akerlof, C. W., et al. 1999, Nature, 398, 400
Band, D., et al. 1993, ApJ, 413, 281
Beloborodov, A. M. 2000, ApJ, 539, L25
Bloom, J. S., et al. 1998, ApJ, 508, L21
Böttcher, M., & Dermer, C. D. 2000, ApJ, 532, 281
Briggs, M., S., et al. 1999, ApJ, 524, 82
Chevalier, R. 1998, ApJ, 499, 810
Chevalier, R., & Li, Z. Y. 1999, ApJ, 520, L29
Connaughton, V. 2002, ApJ, 567, 1028
Costa, E. 2000, in AIP Conf. Proc, 526, Gamma-Ray Bursts: 5th Huntsville Symposium, ed. R. M. Kippen & R. M. Mallozzi (New York: AIP), 365
Dermer, C. D., & Mitman, K. E. 1999, ApJ, 513, L5
Fishman, G. J., et al. 1989, in Proc. Gamma-Ray Observatory Science Workshop, ed. W. N. Johnson (Greenbelt: NASA/GSFC), 2
Ford, L., et al. 1995, ApJ, 439, 307
Fruchter, A., et al. 1999, ApJ, 519, L13
Galama, T., J., et al. 1999, Nature, 398, 394
Galama, T., J., Wijers, R. A. M. J., Bremer, M., Groot, P. J., Strom, R. G., Kouveliotou, C., & van Paradijs, J. 1998, ApJ, 500, L97
Gallant, Y. A., Achterberg, A., & Kirk, J. G. 1999, A&AS, 138, 549
Gallant, Y. A., Achterberg, A., Kirk, J. G., & Guthmann, A. 2000, in AIP Conf. Proc. 526, Gamma-Ray Bursts: 5th Huntsville Symposium, ed. R. M. Kippen & R. M. Mallozzi (New York: AIP), 524
Gehrels, N. 2002, in AIP Conf. Proc., Gamma-Ray Bursts and Afterglow Astronomy 2001, ed. G. Ricker (New York: AIP), in press
Giblin, T., W., Kouveliotou, C., van Paradijs, J., & Fishman, G. J. 1999a, BAAS, 193, 79.06
Giblin, T., W., van Paradijs, J., Kouveliotou, C., Connaughton, V., Wijers, R. A. M. J., Briggs, M. S., Preece, R. D., & Fishman, G. J. 1999b, ApJ, 524, L47
———. 2000, in AIP Conf. Proc. 526, Gamma-Ray Bursts: 5th Huntsville Symposium, ed. R. M. Kippen & R. M. Mallozzi (New York: AIP), 394
Granot, J., & Sari, R. 2002, ApJ, 568, 820
Heinz, S. & Begelman, M. C. 1999, ApJ, 527, L35
Huang, Y. F., Dai, Z. G., & Lu, T. 1999, MNRAS, 309, 513
in't Zand, J. J. M., Heise, G., van Paradijs, J., & Fenimore, J. J. 1999, ApJ, 516, L57
in't Zand, J. J. M., et al. 2001, ApJ, 559, 710
Kobayashi, S., Piran, T., & Sari, R. 1997, ApJ, 490, 92
Kouveliotou, C., Meegan, C. M., Fishman, G. J., Bhat, N. P., Briggs, M. S., Koshut, T. M., Paciesas, W. S., & Pendleton, G. N. 1993a, ApJ, 413, L101

Kouveliotou, C., Paciesas, W. S., Fishman, G. J., Meegan, C. A., & Wilson, R. B. 1992, in Proc. Compton Observatory Science Workshop (Greenbelt: NASA/GSFC), 61
———. 1993b, A&AS, 97, 55
Litvine, D. A., Mitrofanov, I. G., & Kosyrev, A. S. 2000, in AIP Conf. Proc. 526, Gamma-Ray Bursts: 5th Huntsville Symposium, ed. R. M. Kippen & R. M. Mallozzi (New York: AIP), 390
Malkov, M. 1999, ApJ, 511, L53
Mészáros, P., & Rees, M. J. 1997, ApJ, 476, 232
———. 1999, MNRAS, 306, L39
Panaitescu, A. 2001, ApJ, 556, 1002
Pian, E., et al. 2001, A&A, 372, 456
Piran, S. 1999, Phys. Rep., 314, 575
Piro, L., et al. 1998, A&A, 331, L41
Preece, R. D., Briggs, M. S., Mallozzi, R. S., Pendleton, G. N., Paciesas, W. S., & Band, D. L. 2000, ApJS, 126, 19
Preece, R. D., Pendleton, G. N., Briggs, M. S., Mallozzi, R. S., Paciesas, W. S., Band, D. L., Matteson, J. L., Meegan, C. A. 1998, ApJ, 496, 849
Press, W. H., Teukolsky, S. A., Vetterling, W. T., & Flannery, B. P. 1992, Numerical Recipes in C (New York: Cambridge Univ. Press)
Rees, M. J., & Mészáros, P. 1992, MNRAS, 258, P41
Rhoads, J. E. 1999, ApJ, 525, 737
Ryde, F., & Svensson, R. 2002, in Gamma-Ray Bursts in the Afterglow Era, ed. E. Costa, F. Frontera, & J. Hjorth (Berlin: Springer), in press
Sari, R. 2000, in AIP Conf. Proc. 526, Gamma-Ray Bursts: 5th Huntsville Symposium, ed. R. M. Kippen & R. M. Mallozzi (New York: AIP), 504
Sari, R., & Piran, T. 1997, ApJ, 485, 270
———. 1999, ApJ, 520, 641
Sari, R., Piran, T., & Halpern, J. P. 1999, ApJ, 519, L17
Sari, R., Piran, T., & Narayan, R. 1998, ApJ, 497, L17
Schaefer, B. E., & Dyson, S. E. 1995, in AIP Conf. Proc. 384, Gamma-Ray Bursts: 3d Huntsville Symposium, ed. C. K. Kouveliotou, M. S. Briggs, & G. J. Fishman (New York: AIP), 96
Tkachenko, A. Y., Terekhov, O. V., Sunyaev, R. A., Burenin, R. A., Barat, C., Dezalay, J.-P., & Verdenne, G. 2000, A&A, 358, L41
Vietri, M. 1997, ApJ, 488, L105
———. 2000, Astropart. Phys., 14, 211
Vreeswijk, P. M., et al. 1999, ApJ, 523, 171
Waxman, E. 1997, ApJ, 489, L33
Wei, D. M. & Lu, T. 2000, ApJ, 541, 203
Wijers, R., Rees, M., & Mészáros, P. 1997, MNRAS, 288, L51

Note added in proof.—Since the completion of this work, further analysis of GRB 991216 has been performed by V. Connaughton et al. (in Gamma-Ray Burst and Afterglow Astronomy, ed. G. Ricker [Melville: AIP Press; 2002, in press]) that classifies GRB 99126 as a high-energy afterglow candidate. Connaughton et al. have shown that a closer look at the late-time count rates using the orbital background subtraction methods reveals a very low gamma-ray tail lasting several thousand seconds.